ADVANCED ENERGY MATERIALS
www.advenergymat.de

4-Phenylthiosemicarbazide Molecular Additive Engineering for Wide-Bandgap Sn Halide Perovskite Solar Cells with a Record Efficiency Over 12.2%

Padmini Pandey, SungWon Cho, Jitendra Bahadur, Saemon Yoon, Chang-Mok Oh, In-Wook Hwang, Hochan Song, Hyosung Choi, Shuzi Hayase, Jung Sang Cho, and Dong-Won Kang**

The utilization of wide bandgap (WBG) tin halide perovskites (Sn-HPs) offers an environmentally friendly alternative for multi-junction Sn-HP photovoltaics. Nonetheless, rapid crystallization leads to suboptimal film morphology and substantial creation of defect states, which undermine device efficiency. This study introduces 4-Phenylthiosemicarbazide (4PTSC) as an additive to achieve a densely packed Sn-HP film with fewer imperfections. The strong chemical coordination between SnI_2 and the functional groups S═C—N (Sn···S═C—N), $–NH_2$, and phenyl conjugation enhances solution stability and supports the delay of perovskite crystallization through adduct formation. This process yields pinhole-free films with preferred grain growth. 4PTSC acts as a strong coordination complex and a reducing agent to passivate uncoordinated Sn^{2+} and halide ions and reduce the formation of SnI_4, thereby reducing defect formation. The π-conjugated phenyl ring in the 4PTSC facilitates the preferred crystal growth orientation of perovskite grains. Furthermore, the hydrophobic nature of 4PTSC mitigates Sn^{2+} oxidation by repelling moisture, enhancing stability. The open circuit voltage significantly increased from 0.78 to 0.94 V, resulting in achieving the champion efficiency of 12.22% (certified 11.70%), surpassing all previously reported efficiencies for WBG Sn halide perovskite solar cells. Additionally, the unencapsulated 4PTSC-1.0 device maintained outstanding stability over 1200 h under ambient atmospheric conditions.

1. Introduction

Solar energy is recognized as the most copious source of renewable energy, capable of meeting the technological demands of future generations. To date, crystalline-silicon (c-Si) single junction solar cells (SJ-SCs) and various thin film technologies have dominated the global solar industry.[1] The rapidly evolving perovskite solar cell (PSC) technology presents an effective alternative, characterized by easy solution processing, a direct bandgap, tunable bandgap across a wide spectrum, low exciton binding energy (BE) (greater than 20 meV),[2] high absorption coefficient (10^5 cm^{-1}),[3] long-range carrier mobility,[4] and relatively low production costs.[5] Remarkably, within less than twenty years, PSC technology has improved from an initial 3.75% power conversion efficiency (PCE) to a record 26.1%, nearing the Shockley–Queisser limit for SJ-SCs.[6] However, SJ-SCs are limited by optical

P. Pandey, J. Bahadur, D.-W. Kang
Department of Energy Systems Engineering
Chung-Ang University
84 Heukseok-ro, Dongjak-gu, Seoul 06974, Republic of Korea
E-mail: kangdwn@cau.ac.kr

The ORCID identification number(s) for the author(s) of this article can be found under https://doi.org/10.1002/aenm.202401188

DOI: 10.1002/aenm.202401188

S. Cho, S. Yoon, D.-W. Kang
Department of Smart Cities
Chung-Ang University
84 Heukseok-ro, Dongjak-gu, Seoul 06974, Republic of Korea
C.-M. Oh, I.-W. Hwang
Advanced Photonics Research Institute
Gwangju Institute of Science and Technology
Gwangju 61005, Republic of Korea
H. Song, H. Choi
Department of Chemistry
Research Institute for Convergence of Basic Science
Research Institute for Natural Sciences
Hanyang University
Seoul 04763, Republic of Korea

response due to thermalization and transmission losses stemming from their singular bandgap. As a remedy, multijunction solar cells (MJ-SCs) that more efficiently harness photon energy could surpass SJ-SC limitations.[7] Lead (Pb)-based wide bandgap [WBG (E_g≈1.65–1.68 eV)] perovskites have become integral in perovskite/Si MJ-SCs, optimizing light management, and enhancing the open circuit voltage (V_{oc}) of devices.[8] To develop PSC technology as a cost-effective next-generation alternative, significant strides have been made in both academic and industrial sectors. The unmatched optoelectronic properties and high efficiency of PSCs are largely due to the presence of Pb^{2+} ions, despite the environmental concerns related to Pb toxicity. Accordingly, research into alternative materials aims to create environmentally friendly technology without compromising performance. Among various lead substitutes,[9] tin (Sn) halide PSCs have gained attention for their non-toxic nature, similar ionic radii of Sn^{2+} (118 pm) with Pb^{2+} (119 pm),[10] and comparable physical properties. Devices based on Sn halide PSCs have achieved over 14% PCE for narrow bandgap configurations,[11] with WBG (1.6–1.9 eV) sub-cell variants also contributing to V_{oc} enhancements in MJ-SCs.

However, WBG Sn halide PSCs face challenges related to V_{oc} deficits, fill factor (FF) loss,[12] and instability. Developing WBG Sn halide perovskites (Sn-HPs) deals with mixed halide systems, where intrinsic defects form in Sn mixed HPs, due to low solubility and high acidity of Sn precursors[13] leading to defects in the crystal growth process, surface issues causing non-radiative-recombination, deep trap states, moisture sensitivity, and energy band mismatches. The imperfections (charged defects) developed at surface and grain boundaries during the crystal growth process, further drift toward the charge transport layer (CTL)/perovskite interface that could screen the charge extraction at the interface and majorly influence the V_{oc} of the device.[14] The mixed HPs suffer from the formation of an iodine-rich phase (due to phase separation) with a lower bandgap ultimately responsible for V_{oc} deficit in WBG perovskites. Addressing these requires controlling perovskite crystal growth kinetics. Strategies like compositional modification, surface passivation, and molecular additive engineering have been employed to mitigate defects.[15] For instance, additives that form Lewis acid-base adducts can regulate crystallization kinetics, exemplified by using potassium salt of hydroquinone sulfonic acid (KHQSA) and 2-aminophenol-4-sulfonic acid (APSA) to reduce defects in $FASnI_3$.[16] Though several additive molecules have been used separately with specific functionalities such as -C═O, -SO_3, -OH, -NH_2, -S-C, and so on,[17] they could help to regulate the crystal growth kinetics and passivate defects to an extent. However, additives with multifunctionalities can simultaneously regulate the perovskite crystallization through Lewis acid-base adduct with preferred orientation, suppress defect states, and improve long-term stability.

In this work, we endeavored to mitigate the major challenges of WBG Sn-HPs, by understanding the root cause of V_{oc} deficit and non-radiative recombination, we selected multifunctional additives (a bidentate molecule with phenyl conjugation) 4-phenyl thiosemicarbazide (4PTSC) as a precursor additive that not only act as strong Lewis base to develop adduct during perovskite processing, control crystal growth kinetics, suppress non-radiative recombination originates due to mobile ions at surface/grain boundaries by acting as a strong coordinating molecule and reducing agent. The π-conjugated phenyl ring within the 4PTSC promotes the preferential crystal growth orientation of perovskite grains. WBG Sn halide PSCs with exceptional stability and high-power conversion efficiency (PCE) developed. The multifunctional nature of 4PTSC its S-donor, -NH_2 groups, and phenyl ring coordinates with the Sn-HP precursor to control crystal growth orientation and improve crystallinity and stability, resulting in dense, pinhole-free films. The 4PTSC-modified devices not only achieved a peak efficiency of 12.22% (certified at 11.70%) with enhanced V_{oc} but also exhibited superior long-term stability, retaining ≈100% initial PCE after 500 h and ≈80% after 1200 h in ambient conditions. This contrasts with the marked degradation observed in control devices within the first 300 h. Thus, the 4PTSC additive effectively addresses rapid crystal growth, defect formation, and instability in Sn halide PSCs, leading to improved device performance and durability.

2. Results and Discussion

2.1. Effect of 4PTSC Additive on Perovskite Crystallization Process

The effect of 4PTSC additive on the regulation of perovskite crystal growth and grain orientation was explored by using X-ray diffraction (XRD) and field emission scanning electron microscopy (FESEM) analysis. Here, "control" refers to $PEA_{0.15}FA_{0.75}MA_{0.10}SnI_2Br$ (without additive), while 4PTSC-0.5, 4PTSC-1.0 and 4PTSC-2.0 denote 0.5%, 1.0%, and 2.0% 4PTSC additives in $PEA_{0.15}FA_{0.75}MA_{0.10}SnI_2Br$ perovskite, respectively. The composition of our perovskite layer, which includes the large organic molecule phenylethylammonium (PEA^+) cation, is $PEA_{0.15}FA_{0.75}MA_{0.10}SnI_2Br$, leading to the introduction of a quasi-2D perovskite phase. We performed X-ray diffraction (XRD) measurements on both $FA_{0.75}MA_{0.25}SnI_2Br$ (which lacks the PEA^+ cation) and $PEA_{0.15}FA_{0.75}MA_{0.10}SnI_2Br$ films. The XRD patterns, as shown in Figure S1a (Supporting Information), with an expanded view at lower 2θ degrees presented in Figure S1b (Supporting Information), clearly reveal the presence of the quasi-2D phase in the $PEA_{0.15}FA_{0.75}MA_{0.10}SnI_2Br$ perovskite. Lattice parameters calculated for both types of perovskites, detailed in Table S1 (Supporting Information), show approximately similar lattice constants for the 3D perovskite phase. According to previous investigations, the existence of a large n phase (n > 5) in

S. Hayase
i-Powered Energy System Research Center (i-PERC)
The University of Electro-Communications
1-5-1 Chofugaoka, Chofu, Tokyo 182-8585, Japan
S. Hayase
Graduate School of Informatics and Engineering
The University of Electro-Communications
1-5-1 Chofugaoka, Chofu, Tokyo 182-8585, Japan
J. S. Cho
Department of Engineering Chemistry
Chungbuk National University
1 Chungdae-Ro, Seowon-Gu, Cheongju-si, Chungbuk 361-763, Republic of Korea
E-mail: jscho@cbnu.ac.kr

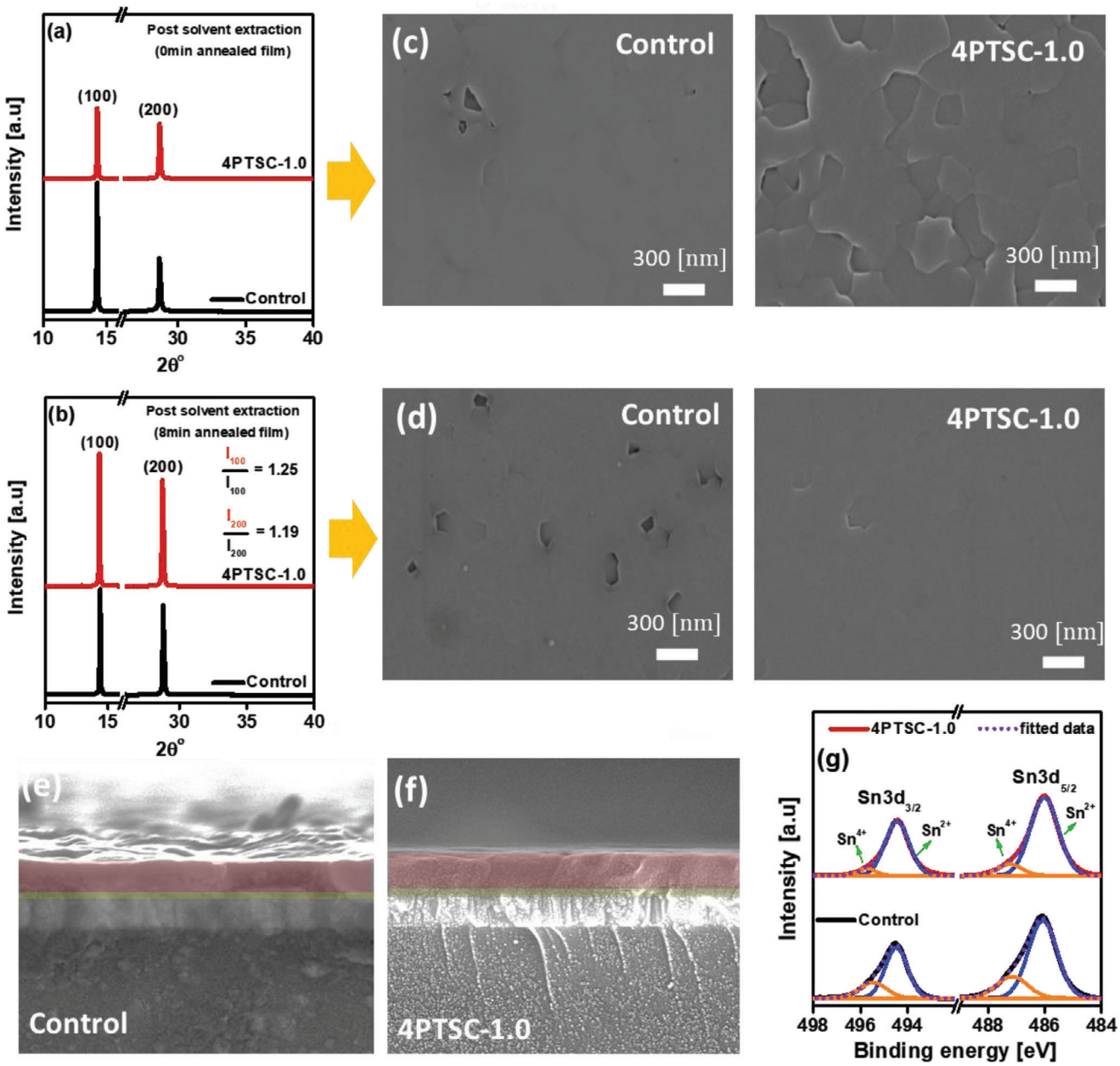

Figure 1. X-ray diffraction (XRD) patterns for control and 4PTSC-1.0 films after anti-solvent extraction step a) 0 min of annealing and b) after 8 min of final annealing. Comparative field emission scanning electron microscopy (FESEM) micrographs for control and 4PTSC-1.0 films after anti-solvent extraction step c) 0 min of annealing and d) after 8 min of final annealing. e,f) Cross-sectional FESEM views of control and 4PTSC-1.0 perovskite films. g) Sn 3d X-ray photoelectron spectroscopy (XPS) core spectra for control and 4PTSC-1.0 films.

mixed 2D–3D perovskites is due to inhomogeneity in processing, and insolubility issues, among other factors. Meanwhile, the formation of a small n-phase is attributed to the presence of a quasi-2D phase near the substrate, which assists in the preferred orientation of the 3D structure,[18] in the present investigation confirmed with Grazing Incidence Wide Angle X-Ray (GIWAXS) as depicted in Figure S2a (Supporting Information). The XRD results indicate the formation of a distinct quasi-2D phase (n = 1), suggesting the presence of a 2D phase, although the dominance of the 3D structure can be readily observed through crystallographic analysis. **Figures 1** and S2c (Supporting Information) illustrate the XRD patterns for the control, 4PTSC-1.0, and perovskite films with different ratios of 4PTSC additive. All perovskite films exhibited similar hkl planes at 14.3° and 28.81° corresponding to the (100) and (200) hkl planes. Based on the XRD analysis, the optimal ratio of 4PTSC was determined to be 1.0%, as shown in Figure S2c (Supporting Information), where the perovskite crystallinity improved with an increase in the additive from 0.5% (4PTSC-0.5) to 1.0% (4PTSC-1.0). However, a significant reduction in film crystallinity was observed for

4PTSC-2.0, confirming that a concentration of 1.0% 4PTSC represents the optimal condition. To investigate the effect of the additive on perovskite crystal growth kinetics, XRD analysis was conducted on both control and 4PTSC-1.0 films at two stages: first, after 0 min of annealing post antisolvent treatment (Figure 1a), and second, after 8 min of final annealing (Figure 1b). The film fabrication process is detailed in the experimental section. As can be seen, the black line depicts the XRD pattern of the control film at 0 min of annealing, which showed a high peak intensity of XRD planes compared to the 4PTSC-1.0 (Figure 1a), indicating faster crystallization of the control perovskite film. This was further confirmed through FESEM as shown in (Figure 1c). Notably, when comparing the film morphology just after antisolvent treatment (0 min of annealing), the control film displayed a smooth surface due to fast crystallization, while 4PTSC-1.0 film morphology depicted an intermediate crystal growth stage, as confirmed through the XRD analysis. Comparing the XRD patterns after 8 min of final annealing (Figure 1b), the peak intensity of (100) and (200) hkl planes substantially increased for the 4PTSC-1.0 perovskite film (red line). The peak intensity ratio of individual peaks I_{100}(4PTSC-1.0)/I_{100}(control) and I_{200}(4PTSC-1.0)/I_{200}(control) was calculated to be 1.25 and 1.19 respectively, indicating that the crystallinity of the 4PTSC-1.0 perovskite film remarkably improved as compared to the control film. The existence of 4PTSC additive plays a pivotal role in influencing the preferred crystal growth orientation of perovskite grains. This phenomenon is further validated by the observed patterns in GIWAXS (4PTSC-1.0 (Target)) as demonstrated in Figure S2b (Supporting Information), providing insights into the crystallographic alignment. The targeted perovskite 2D scattering spectrum (Figure S2b, Supporting Information) reveals pronounced Bragg spots in comparison to the control perovskite film, along the q_z direction at (100) and (200) with q_z values of ≈−2.0 and −0.5 $Å^{-1}$, respectively. These Bragg spots indicate the preferred crystal growth orientation of perovskite when augmented with the 4PTSC additive, showcasing enhanced crystal orientation. Notably, the π-conjugated phenyl ring within the additive exhibits a prominent propensity for rearrangement, particularly at the surface and in the vicinity of perovskite grain boundaries. The concrete evidence underscores the significant impact of the π-conjugated phenyl ring (4PTSC) on guiding and enhancing the crystalline growth orientation of the perovskite material.

Furthermore, we examined the influence of π-conjugated phenyl ring in 4PTSC by comparing the XRD and FESEM of the 4PTSC-1.0 perovskite film with molecular additive thiosemicarbazide (TSC) that lacks a phenyl ring. The XRD patterns are shown in Figure S3 (Supporting Information) for the TSC-assisted perovskite film (TSC-1.0, green line) and 4PTSC-1.0 (red line). The peak intensity significantly improved for 4PTSC-1.0 compared to the TSC-1.0 film. Additionally, the intensity ratio of the (100) and (200) hkl planes, that is, I_{100}(4PTSC-1.0)/I_{100}(TSC-1.0) and I_{200}(4PTSC-1.0)/I_{200}(TSC-1.0) was observed to be ≈1.20 and 1.17, signifying an improved crystal growth orientation of the 4PTSC-1.0 perovskite film. As per previously reported studies, the π-conjugated phenyl ring in the additive promotes the lateral growth of perovskite grains and rearranges at the surface and near perovskite grain boundaries, improving hydrophobicity and thus restricting the absorption of moisture.[19]

The FESEM micrograph of TSC-1.0 is presented in Figure S4 (Supporting Information), in comparison with 4PTSC-1.0. Notably, TSC-1.0 exhibits several pinholes on the film surface, indicative of the presence of surface defects. The FESEM micrographs with a cross-sectional view (taken after 8 min of final annealing) are depicted in Figure 1e,f for the control and 4PTSC-1.0 films. These images reveal uncontrolled crystal growth, the presence of numerous pinholes, and a rough surface observed in the control film (Figure 1d,e) after the final annealing step. This can be attributed to the accelerated growth kinetics, resulting in the formation of an inadequate perovskite film. In contrast, the perovskite film assisted by 4PTSC additive (4PTSC-1.0) exhibits a highly compact, pinhole-free structure, along with a preferred grain orientation and improved crystallinity (Figure 1f). This is likely attributed to the formation of a Lewis acid-base adduct between 4PTSC-Sn halide and the conjugated phenyl ring in 4PTSC.

X-ray Photoelectron Spectroscopy (XPS) analysis was conducted to discern the chemical states and evaluate the inhibition of the Sn^{2+} state in Sn-HP by incorporating 4PTSC-1.0 as an additive. Figure 1g illustrates the Sn 3d XPS core spectra for control (black line) and 4PTSC-1.0 (red line) perovskite films, respectively, calibrated with the BE of ≈284.6 eV (C 1s adventitious peak).[20] Two prominent XPS peaks were identified in the Sn 3d core spectra at 486.11 and 494.53 eV, corresponding to Sn $3d_{5/2}$ and Sn $3d_{3/2}$ (Figure 1g), respectively, for the control perovskite. Additionally, deconvoluted peaks associated with Sn^{4+} and Sn^{2+} oxidation states are indicated. A BE shift of 0.1 eV to ≈486.01 eV (Sn $3d_{5/2}$) and 494.43 eV (Sn $3d_{3/2}$) was observed for the 4PTSC-1.0 perovskite film. The obtained percentages for both states are provided in Table S2 (Supporting Information). The ratio of the Sn^{4+}/Sn^{2+} state for the control is ≈33%; however, a significant reduction to 10.4% in the Sn^{4+} oxidation state was observed for the 4PTSC-1.0 film. The susceptibility to oxidation and the presence of defects on the surface typically arise from uncontrolled growth and excess grain boundaries during film fabrication. This may be a likely explanation for the high ratio of the Sn^{4+} state and pronounced oxidation observed in the control film. We hypothesize that the 4PTSC additive initially regulated the crystal growth kinetics through the formation of a Lewis acid-base adduct between Sn halide and S═C—N, resulting in the formation of a highly crystalline and compact perovskite film with suppressed defect states. The controlled oxidation rate in the 4PTSC-1.0 film can be primarily due to the suppression of surface defects. We posit that S═C—N, -NH_2 functional groups, along with the conjugation of the phenyl ring in the additive, play an essential role in passivating defect states and controlling the oxidation rate by donating electron density to uncoordinated Sn^{2+} ions and inhibiting moisture penetration.

Subsequently, the presence of the 4PTSC additive in the final perovskite film was substantiated through the thermogravimetric analysis (TGA). Comparative TGA plots for the control, 4PTSC powder, and 4PTSC-1.0 perovskite films are depicted in Figure S5 (Supporting Information). The analysis revealed that the 4PTSC additive coexists with the perovskite at an annealing temperature of 70 °C, with a gradual decomposition of the molecule observed at elevated temperatures beyond 180 °C. This experimental finding confirms the establishment of a Lewis acid–base adduct

coordination between the additive and perovskite, which plays a pivotal role in regulating the crystal growth kinetics of perovskite.

2.2. Chemical Coordination and Reducing Effect of 4PTSC with Sn Precursor and Solution Stability

To ascertain the coordination of Sn halides with the 4PTSC additive, comprehensive ^{13}C nuclear magnetic resonance (NMR) studies in the liquid state, alongside Fourier-transform infrared (FT-IR) measurements, were conducted. The ^{13}C liquid state NMR spectroscopy was performed on both 4PTSC and its complex with SnI_2 (4PTSC•SnI_2) in deuterated dimethyl sulfoxide (DMSO-d_6) solution as depicted in **Figure 2a**. The carbon sites, labeled 1–4 in the ^{13}C NMR spectrum, correspond to the chemical shifts associated with the phenyl ring of the additive. The resonance signal at the fifth carbon position, as seen in Figure 2a, is related to the S═C—N functionality within the 4PTSC structure, aligning with the spectral data presented in Figure S6 (Supporting Information). A high-resolution NMR spectrum targeting the specific carbon within the S═C—N functional group is presented in Figure 2b, showcasing a chemical shift at δ = 179.3 ppm for free 4PTSC, in agreement with the reported literature.[21] This shift is observed to change to δ = 178.4 ppm in the 4PTSC•SnI_2 complex (Figure 2b), providing clear evidence of strong chemical coordination (Sn···S═C—N) between the sulfur (S) atom in the S═C—N group and the uncoordinated Sn^{2+} ions, where S-donor with electron lone pair chemically interact with uncoordinated Sn^{2+} ions. This interaction suggests the formation of an adduct during the crystal growth phase, which plays a crucial role in passivating defects and inhibiting Sn oxidation. Considering the -NH_2 functionality in 4PTSC as a hydrogen donor site, we further conducted liquid-state ^1H NMR measurements for 4PTSC, and 4PTSC•SnI_2, to identify -NH_2 hydrogen donor site interactions with iodine (I). The ^1H NMR (600 MHz, DMSO) δ 7.64–7.09 ppm (t, J = 7.4 Hz, ^1H), 4.78 ppm (s, ^1H), 1.07–1.03 ppm (q, J = 6.8 Hz, ^1H) was observed for 4PTSC, while for 4PTSC•SnI_2 complex, a significant chemical shift was observed to ^1H NMR (600 MHz, DMSO) δ 7.56–7.07 ppm (t, J = 7.3, 1.2 Hz, ^1H), 0.95–1.43 ppm (d, J = 7.1 Hz, ^1H), as shown in Figure S7a (Supporting Information). We tested 4PTSC hydrogen bonding with another precursor, FAI (Figure S7b, Supporting Information); the 4PTSC•FAI complex showed a peak shift to 7.62–7.07 ppm (t, J = 7.4 Hz, ^1H), 1.05–1.02 (m, ^1H), indicating H···I interaction in the solution between -NH_2···I with different precursors.

Further substantiating these findings, liquid-state FT-IR spectroscopy was employed. The complete FT-IR spectrum is available in Figure S8 (Supporting Information). Figure 2c,d exhibit comparative FT-IR scans of DMSO, DMSO•SnI_2, DMSO•4PTSC, and DMSO•4PTSC•SnI_2. The spectra demonstrate the absence of any discernible FT-IR signals in samples of DMSO and DMSO•SnI_2 (Figure 2c), whereas distinct peaks at 1275–1280 cm^{-1} and 1212 cm^{-1} are observed in DMSO•4PTSC, corresponding to the S═C stretching vibration (υ_{SC}) and -NH_2 vibrational mode (υ_{NH2}), respectively.[21] The addition of SnI_2 to DMSO•4PTSC, forming DMSO•4PTSC•SnI_2, results in a pronounced redshift of these vibrational modes to approximately υ_{SC} = 1244–1250 cm^{-1} and υ_{NH2} = 1175 cm^{-1} (Figure 2c), corroborating the formation of a substantial Lewis acid-base adduct, 4PTSC•SnI_2. This adduct is likely attributed to the coordination of the S═C—N moiety with Sn^{2+} at the S electron donor site (Sn···S═C—N) and possible hydrogen bonding of the -NH_2 group with halide ions (I^-/Br^-).[15c,17b,22] Additionally, the C—C stretching vibration arising from the phenyl ring conjugation system observed at 1535 cm^{-1} for DMSO•4PTSC (Figure 2d), shifts to 1527 cm^{-1} upon the addition of SnI_2, further confirming the chemical interaction between the phenyl ring of the 4PTSC additive and the SnI_2 precursor.

The Sn^{2+} and X^- ions (I^- in this case) are prone to oxidation to Sn^{4+} and I_2 within a mixed halide system through electron loss.[23] Antioxidant properties, acting as reducing agents, have been established for semicarbazide and thiosemicarbazide derivatives in prior studies.[24] The coordination of 4PTSC with SnI_2 was identified via NMR and FT-IR analyses. To further assess the reducing efficacy of the 4PTSC additive, cyclic voltammetry (CV) measurement was conducted. These measurements were performed in a solvent mixture of DMF:DMSO (4:1), with the experimental setup and analysis details provided in the Supporting Information. A comparative CV profile for SnI_2 and 4PTSC•SnI_2 is illustrated in Figure S9 (Supporting Information), showing that SnI_2 exhibits an anodic peak potential ($E_{p.a}$) at −0.82 V (vs Ag/Ag^+) and a cathodic peak potential ($E_{p.c}$) at −1.20 V (vs Ag/Ag^+), indicative of a quasi-reversible process with a midpoint potential ($E_{1/2}$) of −1.01 V. In the SnI_2 solution, a cathodic peak at −0.76 V (vs Ag/Ag^+) suggests the $E_{p.c}$ for SnI_4. Furthermore, the CV profile of 4PTSC•SnI_2 reveals an $E_{p.a}$ peak at −0.72 V (vs Ag/Ag^+) and an $E_{p.c}$ at −1.20 V (vs Ag/Ag^+), with an $E_{1/2}$ of −0.97 V. The anodic potential range of −0.75–−1.0 V (vs Ag/Ag^+) is deemed suitable for an additive to act as a reducing agent, facilitating the conversion of SnI_4 to SnI_2.[25] In SnI_2, both Sn^{2+} and I^- are susceptible to oxidation through electron loss.[26] The 4PTSC additive, featuring an S═C electron donor system, interacts with uncoordinated Sn^{2+} ions, while its -NH_2 acts as a hydrogen donor site, potentially serving as a sacrificial reductant. An additive processing of an NH-NH_2 hydrogen donor is capable of donating electrons, thus preventing the oxidation of I^- ions.[27] Notably, the CV analysis of 4PTSC•SnI_2 did not display a cathodic peak for SnI_4 (Figure S9, Supporting Information), implying that 4PTSC also serves as a reducing agent for Sn-HP.

The stability of the solutions, comprising bare SnI_2 in a DMF:DMSO mixture and those containing varying mole percentages of the 4PTSC additive was monitored. A visual comparison of the solution stability of SnI_2 with different concentrations of 4PTSC is presented in Figures 2e and S10 (Supporting Information), wherein the color transformation of the bare SnI_2 solution from pale to dark yellow within 40 h, proceeding to a brown hue over 100 h, is indicative of the oxidative interaction of Sn^{2+} ions with atmospheric oxygen. A schematic representation detailing the potential degradation pathways in SnI_2 and the chemical coordination between the 4PTSC additive and SnI_2, as well as the reductive behavior of 4PTSC, is delineated in Figure 2f,g. Figure 2f depicts the oxidation process of SnI_2, leading to the conversion of Sn^{2+} to Sn^{4+} and $2I^-$ to I_2. This conversion, resulting in the formation of uncoordinated Sn^{2+} and halide ions, leads to non-radiative recombination losses, distorting the perovskite structure and diminishing its stability. Figure 2g demonstrates the chemical coordination and reductive behavior of the 4PTSC additive upon interacting with SnI_2. The 4PTSC consists of

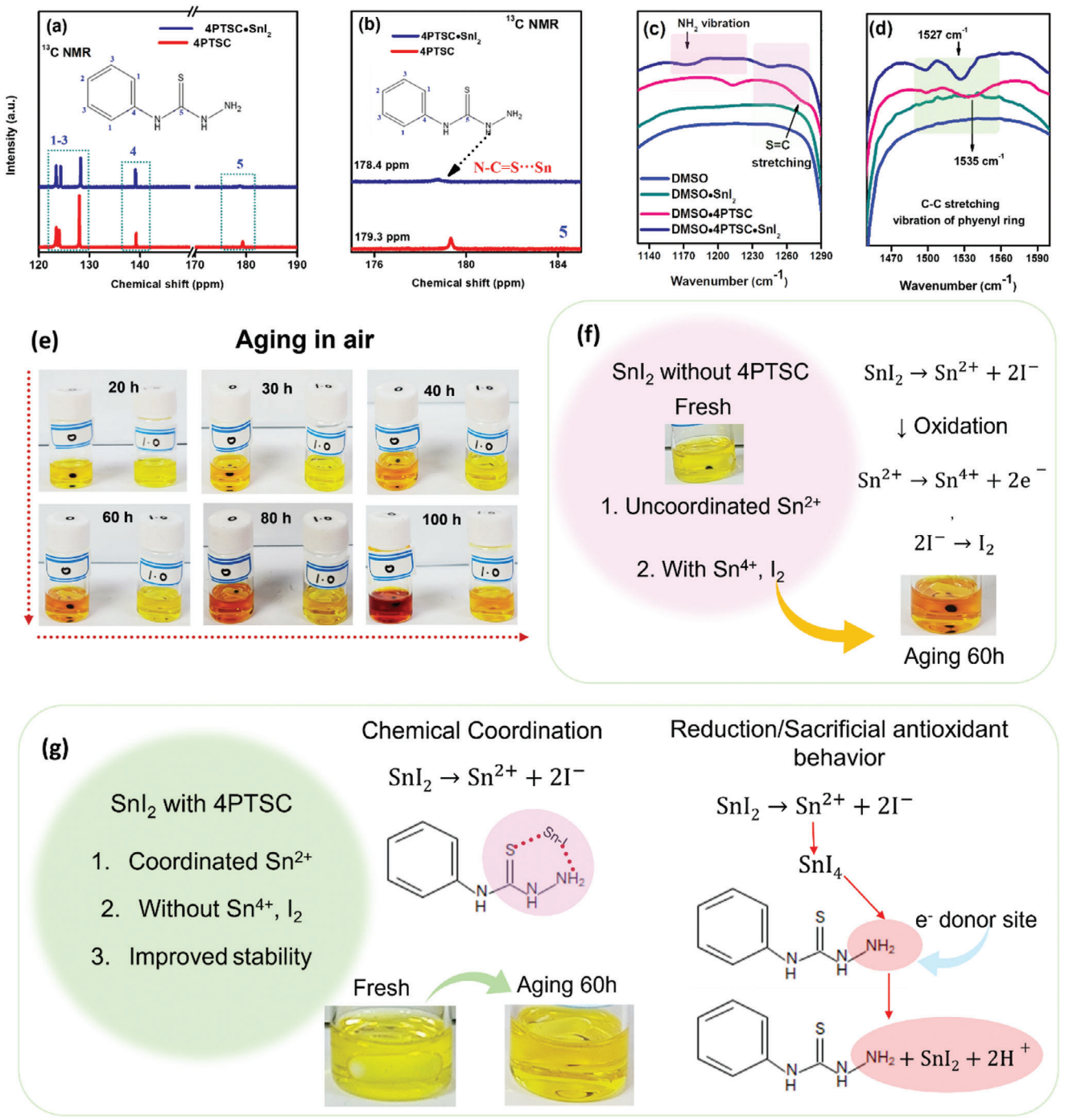

Figure 2. a,b) Comparative ^{13}C NMR spectra of 4PTSC additive and the 4PTSC•SnI_2 complex in deuterated DMSO (DMSO-d_6). c,d) Fourier-transform infrared (FT-IR) spectroscopy comparative analysis depicting the spectral regions corresponding to -NH_2 and S = C stretching modes c) and C-C stretching resonances d), for DMSO, DMSO•SnI_2, DMSO•4PTSC, and DMSO•4PTSC•SnI_2. e) Graphical depiction of the temporal stability of SnI_2 in the presence of ambient air for a period of 100 h; for DMF:DMSO•SnI_2 (denoted as '0') and DMF:DMSO•4PTSC•SnI_2 (denoted as '1.0'). f) Schematic illustration detailing SnI_2 oxidation. and g) Schematic illustration detailing the chemical coordination interactions and reducing property of 4PTSC additive with SnI_2.

multifunctional groups including a phenyl ring, S═C—N linkage, and -NH_2 nucleophiles. The S═C—N moiety engages with the uncoordinated Sn^{2+} ions (Sn···S═C—N), preventing oxygen from interacting with the perovskite surface and reducing the likelihood of deep trap state formation. Experimental evidence supports strong chemical coordination between SnI_2 and the Lewis base functionalities of 4PTSC (Figure 2g). The resultant Lewis acid-base adduct between 4PTSC and SnI_2 is conjectured to modulate the crystal growth kinetics favorably, ultimately leading to the development of a highly compact and crystalline perovskite film, as shown in Figure 1 for the sample with 1.0 mole% 4PTSC (denoted as 4PTSC-1.0). As clearly visible in Figure 2e, the incorporation of the 4PTSC-1.0 additive enhances the stability of the SnI_2 precursor solution. The oxidation of I^- to I_2 poses another stability challenge for SnI_2. The 4PTSC molecule contains another nucleophilic site, -NH_2, which could mitigate the oxidation of SnI_2 and inhibit ion migration through forming hydrogen bonds (NH_2-···I), as shown in Figure 2g, or act as a reducing agent by donating electrons to revert SnI_4 back to the SnI_2 state,[19c,27,28] thereby improving the stability of SnI_2. These observations suggest that the multifunctional nature of the 4PTSC additive coordinates with SnI_2 to form a robust Lewis acid-base adduct. The electron-donating group (-NH_2) in 4PTSC donates electrons to stabilize SnI_2 in the solution, functioning as a reducing agent, while the conjugated phenyl groups enhance the solution's overall stability.

To corroborate the dual role of the phenyl conjugation in not only enhancing crystallinity and grain orientation (as evidenced in Figure 1) but also in inhibiting the oxidation of Sn^{2+} ions (as seen in **Figures 1** and **2**), an open-air solution stability assay was conducted. SnI_2 (0), SnI_2•TSC (TSC-1.0), and SnI_2•4PTSC (4PTSC-1.0) were subjected to stability testing in a DMF: DMSO matrix under ambient conditions with a relative humidity of 40%, as demonstrated in Figure S11 and Video S1 (Supporting Information). It was observed that while clear oxidation occurred within 2 min for the solutions without 4PTSC additive, the inclusion of 4PTSC (4PTSC-1.0) significantly mitigated the impact of air and moisture up to a duration of 4 min. The 4PTSC is comprised of multifunctional attachments. The C-H in the phenyl ring has a relatively small electronegativity difference, hence the electrons in the bonds are shared equally between C and H and there is zero electronegativity difference between C-C. Hence there is no charge separation and polarity on the aromatic phenyl ring. This non-polar behavior makes it hydrophobic and could retard moisture diffusion in perovskite.[29] The enhanced stability in the presence of the 4PTSC additive underlines the protective effect afforded by the superior hydrophobic nature of the aromatic rings.

2.3. Defect Passivation and Plausible Mechanism

The density of defect states within HPs critically influences charge carrier dynamics and the overall performance of PSCs. To elucidate the effect of 4PTSC additives on the light absorption properties and charge carrier dynamics within the perovskite structure, a series of optical characterizations were conducted. These included UV–vis absorbance, steady-state (SS) and time-resolved photoluminescence (TRPL), and transient absorption spectroscopy (TAS). The absorption spectra of control and 4PTSC-1.0-incorporated perovskite films are shown in Figure S12a (Supporting Information), where no discernible shift in the absorption edge between the films was observed, indicating that the inclusion of 4PTSC-1.0 does not alter the bandgap of the perovskite (E_g = 1.65 eV as calculated from the Tauc plot in Figure S12b, Supporting Information). Ultraviolet photoelectron spectroscopy (UPS) was employed to determine the effect of additive engineering on the valence band maxima (VBM) positions and band alignments, with results presented in **Figure 3a**. Work function "ϕ" values, determined using Equation S1 (Supporting Information)[30] were found to be ≈−4.47 eV for the control and −4.39 eV for the 4PTSC-1.0 sample. Moreover, the calculated positions of the VBM and conduction band minima (CBM) for the control perovskite were −5.93 eV (−4.28 eV), and for the 4PTSC-1.0-modified perovskite were −5.35 eV (−3.70 eV), with band energy level alignments presented in Figure 3b. The VBM for the control sample is at ≈−5.93 eV, and the lowering of VBM in Sn-HPs to −5.9–6.0 eV is ascribed to the dominant Sn^{4+} states.[31] This indicates severe oxidation of the perovskite surface and dominance of the Sn^{4+} oxidation state, in agreement with the XPS results (Figure 1g control) as stated above. The VBM upshifted to −5.35 eV in 4PTSC-1.0, which signifies a suppressed oxidation rate of Sn^{2+}, which is in good agreement with the XPS analysis (reduction in Sn^{4+} ratio in 4PTSC-1.0 film). The electron lone pair at S═C—N could help in reducing the oxidation rate by localizing the density of electrons around Sn ions, chemically coordinating with the uncoordinated Sn^{2+}. The -NH_2 donor site could help in reducing the ion migration by forming H···I bond and suppressing the formation of SnI_4 by acting as a reductant. This helps in controlling the oxidation rate and simultaneously adjusting the band energy levels for efficient charge transport. Additionally, the phenyl ring in 4PTSC could passivate the grain boundaries, thus reducing extended defects (mobile ions) and improving perovskite stability.[32]

The SSPL spectrum at an excitation wavelength (λ_{ex}) of 470 nm, shown in Figure 3c, reveals an augmented PL intensity for the 4PTSC-1.0 film compared to the control, indicating successful defect passivation, and diminished non-radiative recombination through additive engineering. A clear blue shift in the PL emission peak (λ_{em} = 750 nm) was observed for 4PTSC-1.0, which indicates the passivation of defect states within the bandgap of perovskite, by influencing the crystal growth kinetics leading to the formation of highly compact perovskite film with suppressed non-radiative recombination losses.[32c,33] The TRPL (Figure 3d) analysis of the films deposited on glass substrates revealed a prolongation of the average carrier lifetime from 22.5 ns for the control to 39.6 ns for the 4PTSC-1.0 film, indicative of a substantial reduction in defect states within the perovskite matrix due to the 4PTSC additive.

Femtosecond-TAS (fs-TAS) was further employed to substantiate the defect passivation in 4PTSC-1.0. Figure 3e depicts the fs-TAS profiles at a 650 nm photoexcitation and a pump influence of 1 μJ cm^{-2}, captured at time delays ranging from 1 to 1000 ps. A pronounced ground-state bleach signal within the 730–750 nm region, identified as a photoinduced transient bleach (PIB) state, correlates with the E_g of perovskite as verified in Figure S12b (Supporting Information). The PIB spectral intensity in the 4PTSC-1.0 modified film diminishes more slowly

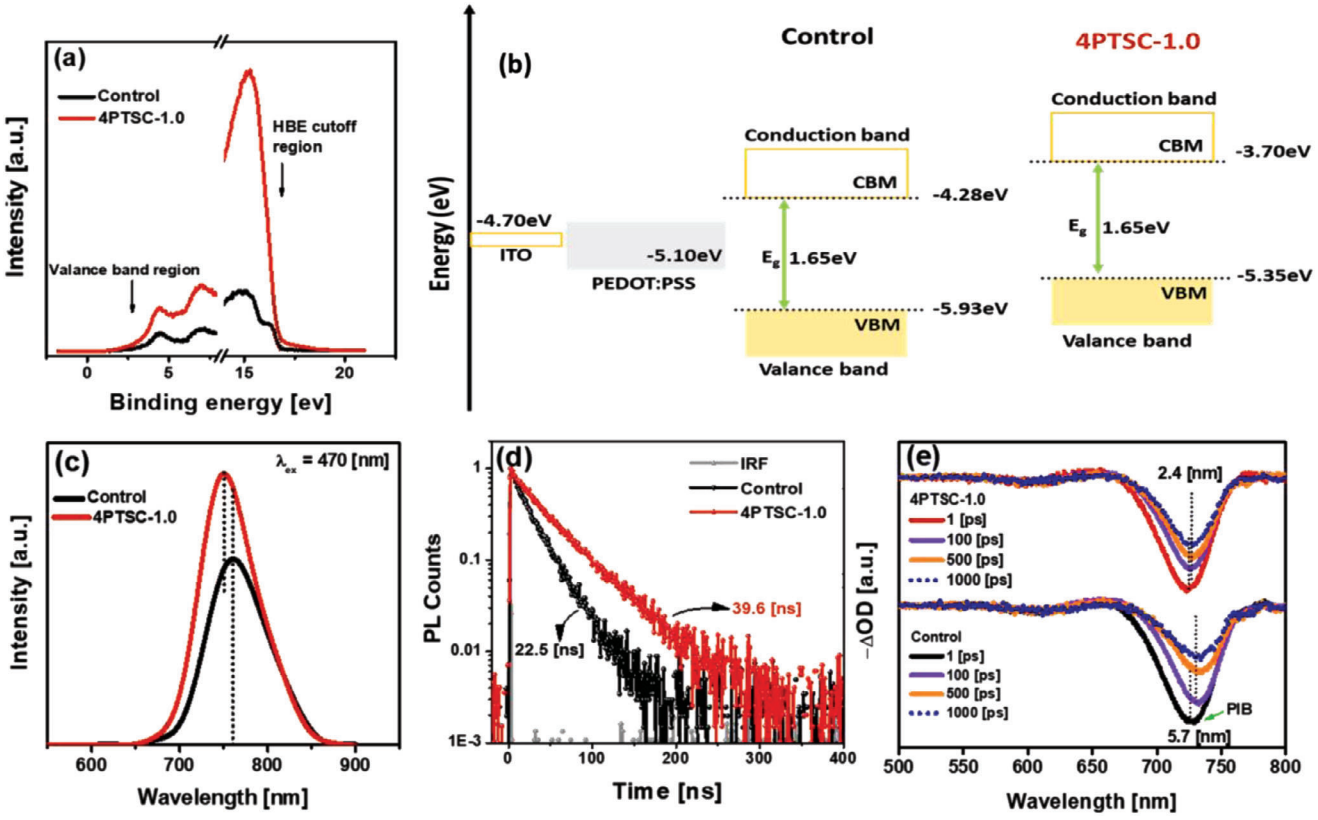

Figure 3. a) Ultraviolet Photoelectron Spectroscopy (UPS) spectra for control and 4PTSC-1.0 with assigned high binding energy (HBE) cutoff and valance band region. b) Band energy alignment illustration for control and 4PTSC-1.0 with respect to the hole transport layer (HTL). c) Steady-state photoluminescence (SSPL), d) time-resolved (TRPL) spectroscopy, and e) Femtosecond-transient absorption spectroscopy (fs-TAS) ΔOD as a function of wavelength at several time delays at photoexcitation wavelength of 650 nm (pump fluence of 1 μJ cm^{-2}) analysis of control and 4PTSC-1.0 perovskite films.

than in the control, indicating fewer defects in the former.[34] At a 1 ps optical delay, the PIB signal emerged at 724.8 nm for both control and 4PTSC-1.0 films. However, as the optical delay progressed, the PIB signal for the control film displayed a redshift, the initial band at 724.8 nm exhibited a red shift to 727.2 nm. The early-stage band shift suggests a renormalization of E_g, in the control film, the shift in the band edge is possibly attributed to defect states within the bandgap. Specifically, upon photoexcitation, excited carriers populate trap states, resulting in a redshift of the photoinduced transient bleach (PIB) signal as a function of delay time. Notably, for the target 4PTSC-1.0 perovskite film, renormalization is observed at the initial stage, with a constant peak position maintained across various time delays. This evidence suggests that enhanced coordination between additive functionalities and perovskite mitigated the defect states in the 4PTSC-1.0 perovskite film.

The experimental evidence leads us to propose a plausible schematic for the crystallization mechanism and defect passivation. The intricate fabrication of WBG Sn-HPs involves complexities within mixed halide systems, where intrinsic defects manifest due to the low solubility and high acidic characteristics in Sn precursors. This interplay culminates in detrimental defects during the crystal growth process, worsening issues such as crystal growth imperfections, uncoordinated Sn^{2+}, and halide ions leading to surface-related non-radiative recombination, deep trap states, sensitivity to moisture-induced degradation, and so on (**Figure** 4a). However, upon meticulous examination of the challenges associated with WBG Sn-HP, our present study adopts a distinctive approach. The wet perovskite film before antisolvent treatment, as depicted in Figure 4b, demonstrates the chemical coordination of Sn halide with the 4PTSC additive (4PTSC-1.0). The incorporation of 4PTSC results in S═C─N and -NH_2 groups chemically coordinating with Sn halide, forming a strong Lewis acid-base adduct. Antisolvent treatment applied to the wet films induced a supersaturated state, initiating perovskite nucleation. Subsequently, the adduct (4PTSC•SnX_2/PEAFAMA) stabilized the intermediate perovskite phase and regulated the rate of crystal growth. Conversely, the control films (Figure 4a) experienced rapid crystallization upon antisolvent treatment, a consequence of the strong Lewis acidity of Sn halide precursors, which ultimately yielded films of inferior quality. During the final annealing at 70 °C for 8 min, the controlled films exhibited defects such as surface non-uniformity, random orientation, point defects, and oxidation due to unregulated crystal growth kinetics. Conversely, the 4PTSC-1.0 film displayed a dense and uniform crystal grain growth upon final annealing. Our findings confirm the presence of the 4PTSC additive in the annealed perovskite film, which effectively passivates defects, thereby mitigating

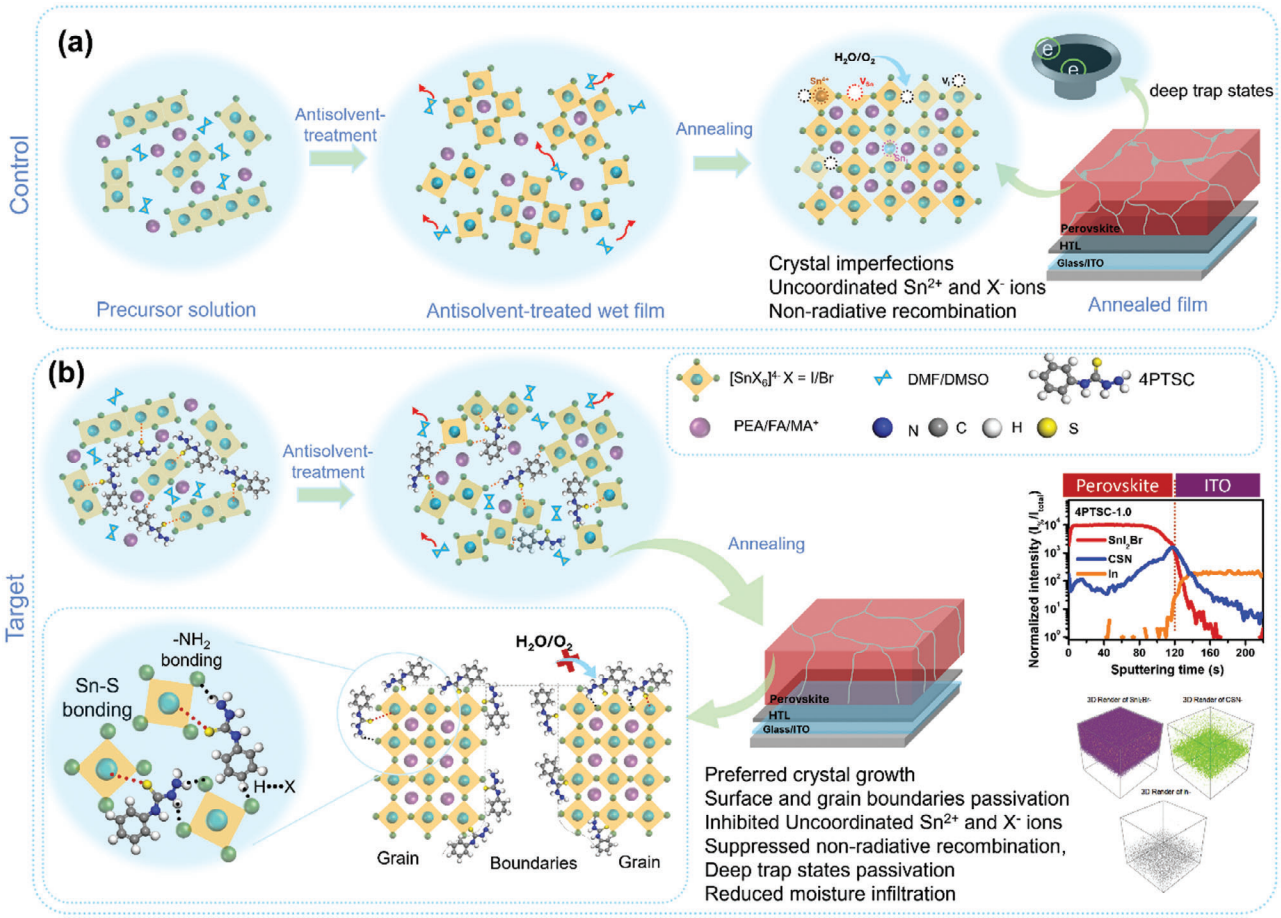

Figure 4. Schematic illustration a) Challenges associated with WBG Sn mixed halide Control perovskite. b) Plausible schematic illustration of the chemical coordination of 4PTSC additive with the perovskite precursor during the initial stages of crystal growth modulation, defect passivation, and stabilization of the perovskite phase through Sn^{2+} coordination. The presence of 4PTSC was affirmed through Time-of-Flight Secondary Ion Mass Spectrometry (ToF-SIMS). 4PTSC molecule additive effectively passivates surface and grain boundaries and regulates the crystal growth orientation.

non-radiative recombination. Beyond its role as a potent Lewis base coordinating adduct formation, 4PTSC unveils additional properties by serving as a reducing agent and regulating the kinetics of perovskite crystallization. Its molecular architecture boasts a rich collection of functionalities, including an S═C─N linkage, -NH_2 nucleophiles, and phenyl ring conjugation. In the current investigation, we deliberately employed a multifaceted molecule, demonstrating exceptional efficacy as a Sn precursor additive. Profound chemical coordination develops between SnI_2 and the Lewis base functionalities of 4PTSC. The S═C─N moiety actively engages with uncoordinated Sn^{2+} ions (Sn···S═C─N) via electrostatic interactions, effectively shielding the perovskite surface from oxygen interaction and thereby attenuating the propensity for deep trap state formation. Our investigation also addresses the challenge of halide oxidation (I^- to I_2), a substantial concern for SnI_2. Here, the -NH_2 nucleophilic site within 4PTSC emerges as a strategic solution, suppressing the oxidation of SnI_2 and impeding ion migration through the formation of hydrogen bonds (-NH_2···I). Simultaneously, it operates as a potent reducing agent, donating electrons to reverse SnI_4 to the SnI_2 state, thereby sustaining the stability of SnI_2 and potentially passivating negatively charged defects. While the π-conjugated phenyl ring within the additive undergoes rearrangement at the surface and in proximity to perovskite grain boundaries as depicted in Figure 4b ToF-SIMS image, facilitates the preferred crystal growth orientation of perovskite grains (as shown in XRD (Figure 1b) and GIWAXS (Figure S2b, Supporting Information). The non-polar characteristics of this phenyl ring render it hydrophobic, persistently limiting moisture absorption. Consequently, the multifunctional attributes of the 4PTSC additive compose the establishment of a strong Lewis acid-base adduct with SnI_2. The electron-donating ability of the (-NH_2) group within 4PTSC actively stabilizes SnI_2 in the solution, operating as an effective reducing agent, collectively suppressing non-radiative defect formation. Simultaneously, the conjugated phenyl ring promotes a preferred crystal growth orientation, thereby improving the overall stability of the perovskite system.

2.4. WBG Sn Halide Perovskite Solar Cell Device Study

The photovoltaic devices were constructed using an inverted p-i-n device architecture, consisting of ITO/PEDOT:PSS/WBG Sn-HP/PCBM/BCP/Ag layers, with detailed fabrication procedures

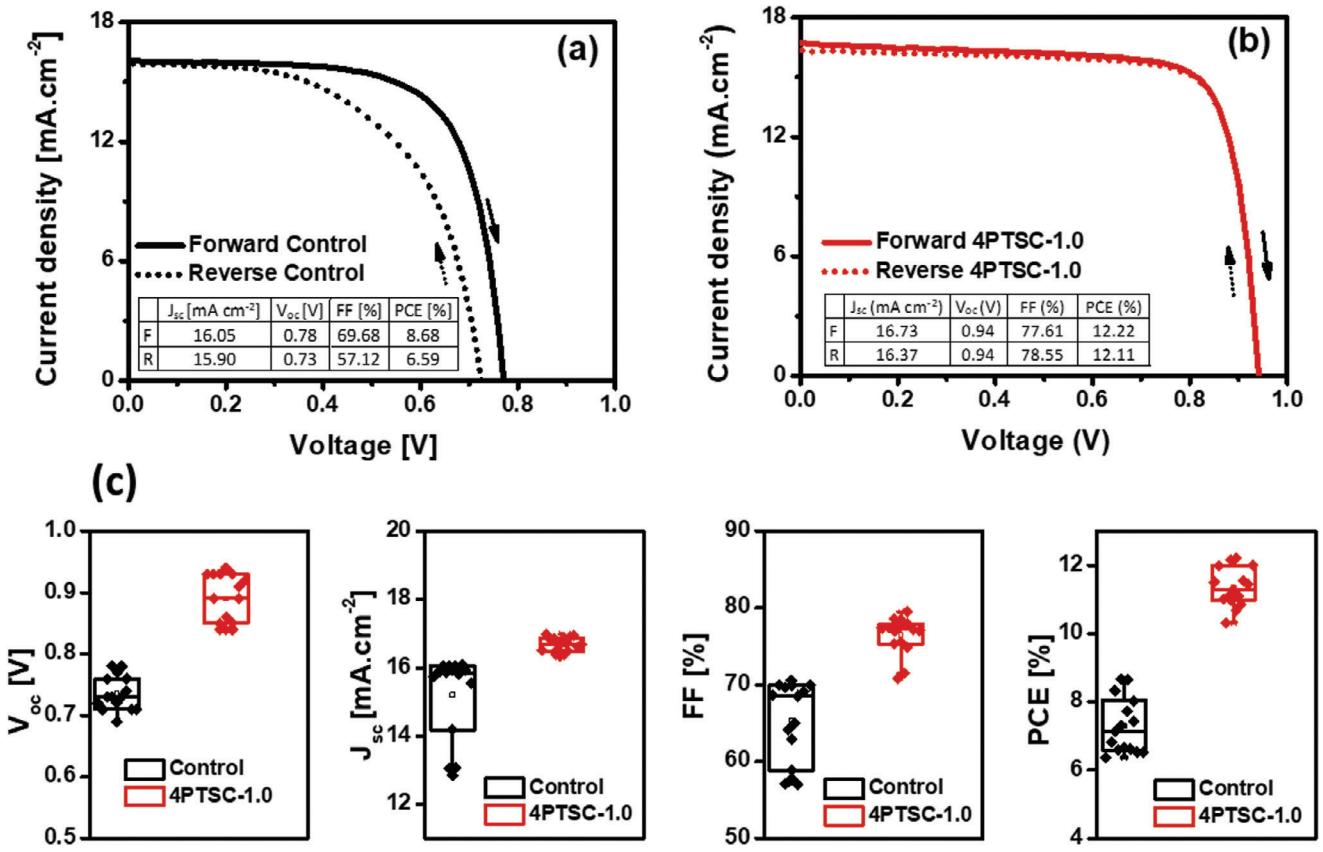

	J_{sc} [mA cm^{-2}]	V_{oc} [V]	FF [%]	PCE [%]
F	16.05	0.78	69.68	8.68
R	15.90	0.73	57.12	6.59

	J_{sc} (mA cm^{-2})	V_{oc} (V)	FF (%)	PCE (%)
F	16.73	0.94	77.61	12.22
R	16.37	0.94	78.55	12.11

Figure 5. Current density versus voltage (*J–V*) curves of a) control device, b) 4PTSC-1.0 champion device in forward and reverse scans c) Statistical distributions and comparative graphs of various device parameters extracted from *J–V* characteristic curves for control and 4PTSC-1.0 devices.

outlined in the experimental section. **Figure 5**a,b illustrate the current density (J) versus voltage (V) characteristics of the 4PTSC-1.0-based devices compared to the control PSCs, measured in both forward and reverse scans under AM 1.5 illumination. The associated solar device parameters are presented in Table S3 (Supporting Information). The current–voltage (*J–V*) characteristic curves of the WBG Sn halide PSCs with varying concentrations of the additive are depicted in Figure S13 (Supporting Information). The control PSC exhibited a PCE of 8.68%, with a J_{sc} of 16.05 mA cm^{-2} and a V_{oc} of 0.78 V, alongside noticeable hysteresis. The ionic mobility in halide perovskites, which can encourage photoinduced phase segregation, ion migration, and instability,[35] is exacerbated by morphological imperfections in the control perovskite film (see Figure 1c,d), leading to defect mobilization under an electric field and resultant hysteresis. In contrast, the 4PTSC-1.0 WBG Sn halide device showcased remarkable performance, achieving an exceptional PCE of 12.22% for the champion device with a V_{oc} of ≈0.94 V, a J_{sc} of 16.73 mA cm^{-2}, and an FF of 77.61%, representing the highest reported PCE for WBG Sn halide PSCs to date, with a certified performance of 11.7% (refer to Figure S14, Supporting Information). Furthermore, Figure S15 (Supporting Information) showcases the PCE versus bandgap and the yearly distribution of PCE for WBG Sn halide PSCs. Additionally, a comparative analysis of the current record efficiency with prior studies is presented in Table S4 (Supporting Information). The lower V_{oc} observed in the control PSC can likely be attributed to defect states associated with the Sn^{4+} condition, while the reduced V_{oc} deficit and enhanced FF in the 4PTSC-1.0 device indicate a significant suppression of non-radiative recombination, improved surface morphology, enhanced crystallinity, and reduced oxidation of Sn^{2+} within the perovskite structure. Notably, the 4PTSC-1.0 PSC demonstrated negligible hysteresis, indicating inhibited ion migration. Contrary to the control perovskite, the -NH_2 functional groups in 4PTSC-1.0, interacting with halide ions through hydrogen bonding, appear to effectively mitigate photoinduced ion migration. It is understood that this additive, namely 4PTSC, serves dual functions as both a coordination complex and a reducing agent, effectively addressing the issues of non-radiative recombination, uncoordinated Sn^{2+} and halide ions, and the oxidation of perovskite. We are confident that such strategic utilization of specific multifunctional additives with selective functionalities can significantly enhance the V_{oc} of WBG Sn-HPs. Most importantly, this additive strategy preserves the bandgap of WBG Sn-HPs, offering great promise for the future advancement of WBG Sn halide PSCs. In essence, by maintaining the desired WBG, we are able to counteract non-radiative recombination caused by mobile ions at the surface and grain boundaries. The multifunctional additives act not only as strong Lewis bases, promoting adduct formation during perovskite processing and influencing crystal growth kinetics, but also as sacrificial reductants.

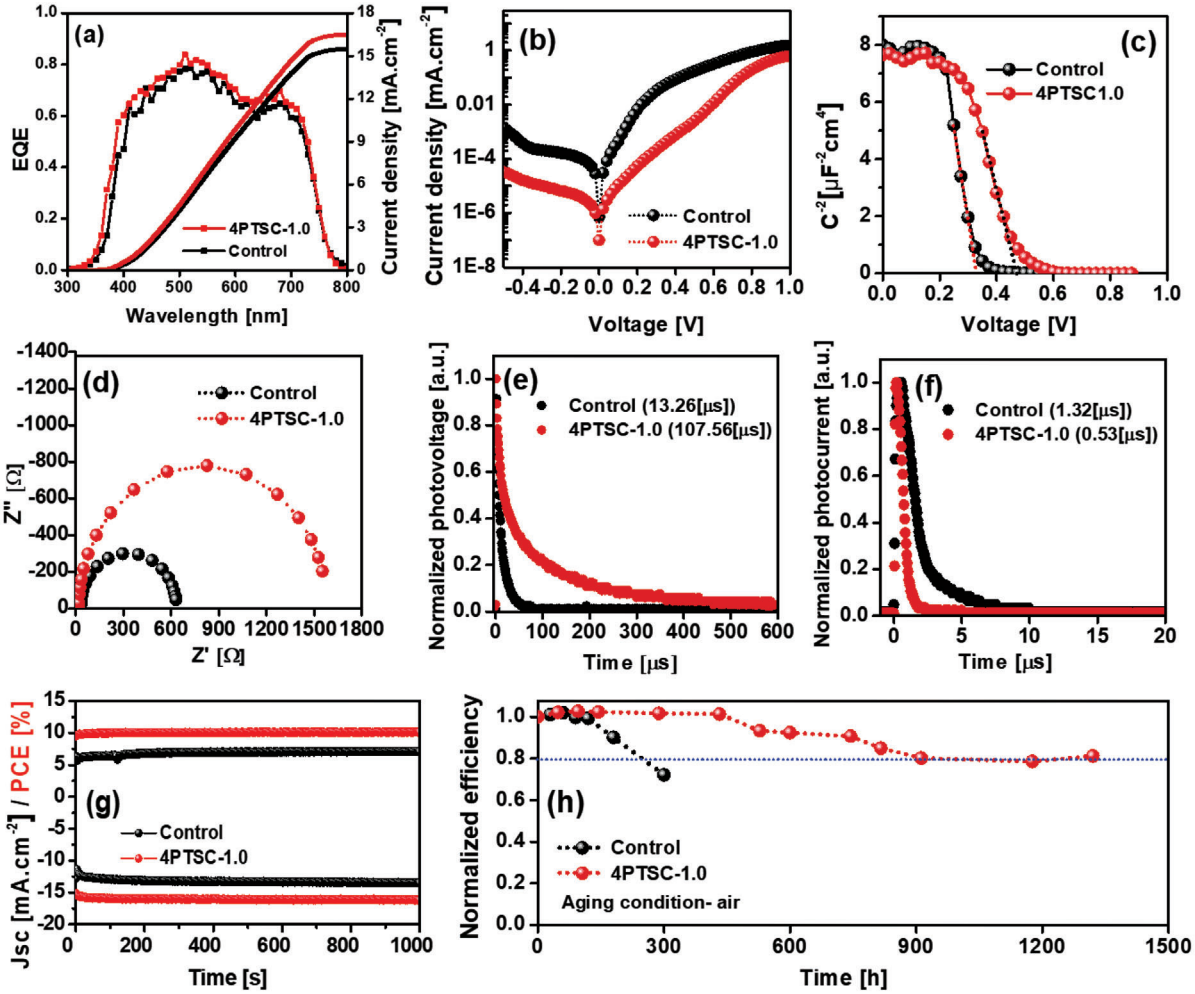

Figure 6. a) External quantum efficiency (EQE) spectrum with integrated J_{sc}, b) dark *J–V* curves, c) Mott–Schottky (M–S) curves, d) Electrochemical Impedance Spectroscopy (EIS) Nyquist plots for control (black line) and 4PTSC-1.0 (red line) device respectively. e,f) Transient photovoltage (TPV) and transient photocurrent (TPC) graphs for control and 4PTSC-1.0 devices. g) Stabilized power output (SPO), h) Ambient air stability graph at 30%–40% relative humidity (RH) for control, and 4PTSC-1.0 device without any encapsulation.

To verify the consistency of device performance, statistical data were collected for a set of 15 devices for both the control and 4PTSC-1.0 configurations, as illustrated in Figure 5c. Additional statistical data for the 4PTSC-0.5 and 4PTSC-2.0 variants are presented in Figure S16 (Supporting Information). The J_{sc} values were corroborated through external quantum efficiency (EQE) analysis (**Figure 6a**), with the integrated J_{sc} measuring 15.48 mA cm^{-2} for the control and 16.47 mA cm^{-2} for the 4PTSC-1.0 PSC, matching well with the J_{sc} values derived from the *J–V* curves. The EQE spectrum indicates a marginal enhancement in light harvesting for the 4PTSC-1.0 device, suggesting that the inclusion of the 4PTSC additive positively impacts charge carrier generation within the perovskite structure.

To further assess the impact of 4PTSC additive on charge transfer dynamics, dark *J–V* characteristics, and electrochemical impedance spectroscopy (EIS) were conducted, as shown in Figure 6. The dark *J–V* analysis revealed a lower saturation current for the 4PTSC-1.0 variant (Figure 6b), which correlates with an increase in the device's V_{oc} when compared to the control PSC. This reduced saturation current, indicative of decreased defect states within the 4PTSC-1.0 perovskite, leads to a diminished V_{oc} deficit.[36] This decrease in defect density is further elucidated through Mott–Schottky (M–S) analysis using capacitance–voltage (C–V) measurements (Figure 6c), with defect density (N_d) calculated using Equation S2 (Supplementary Information).[37] N_d values derived from the M–S data exhibit a marked decline from 2.39 × 1012 cm^{-3} for the control to 6.75 × 10^{10} cm^{-3} for the 4PTSC-1.0, substantiating the role of the 4PTSC additive in effectively mitigating defect states within the perovskite. EIS measurements were performed to evaluate the recombination processes within the devices, as depicted in Figure 6d. The recombination resistance (R_{rec}) for the control device was found to be 627 Ω, which increased to ≈1554 Ω for the 4PTSC-1.0 device, indicating minimized defect-assisted trap states that could impede charge carrier recombination. Charge carrier recombination and transport properties were further examined through transient photovoltage (TPV) and photocurrent (TPC) measurements, as illustrated in Figure 6e,f. An extended recombination lifetime

(τ_{rec}) of 107.56 µs for 4PTSC-1.0, compared to 13.26 µs for the control, was observed in Figure 6e. This finding is consistent with the significant reduction in defect state density and aligns with results from optical analysis and EIS. Charge carrier lifetime (τ_{ct}) was estimated to be ≈1.32 µs for the control perovskite, while a faster decay was observed for 4PTSC-1.0 (τ_{ct} = 0.53 µs), as shown in Figure 6f, confirming efficient charge extraction and transport for photo-generated carriers.[22,38] Thus, the 4PTSC-1.0 perovskite device demonstrates enhanced charge dynamics and suppressed non-radiative recombination, leading to improved V_{oc} and FF.

Figure 6g presents the stabilized power output (SPO) profiles for the control and 4PTSC-1.0 devices at the maximum power point (MPP), under continuous illumination for 1000 s at 1 Sun. The SPO for the control device registered at 7.07%, whereas the 4PTSC-1.0 device achieved 10.1%, indicating that a strategic reduction of defects can significantly augment SPO during prolonged exposure. The durability of the unencapsulated control and 4PTSC-1.0 devices was documented under ambient conditions with 30% relative humidity, as shown in Figure 6h. The control device exhibited rapid degradation within 300 h under high humidity conditions, whereas the 4PTSC-1.0 device maintained near-total PCE retention for over 500 h. After 1200 h, the 4PTSC-1.0 device sustained ≈80% of its initial performance, demonstrating its exceptional stability.

3. Conclusion

In conclusion, the study presents an additive engineering approach that facilitates the formation of adducts in the precursor solution, augments solution stability, modulates the dynamics of crystal growth, mitigates defect states, and interacts chemically with uncoordinated Sn^{2+} ions to prevent their oxidation, thereby enhancing the performance and operational stability of the device while minimizing V_{oc} losses. The 4PTSC additive demonstrates effective governance over the kinetics of Sn-HP crystallization and solution stability. This governance is attributed to the strong chemical coordination of SnI_2 with S═C─N, -NH_2 functional groups, and the phenyl ring structure of 4PTSC, which collectively directs the crystal growth directionality, fostering the formation of a highly compact perovskite layer. Concurrently, delayed crystallization serves to curtail imperfections. The study elucidates that the 4PTSC additive curbs the generation of defect states through chemical interactions with uncoordinated Sn^{2+} ions, arresting Sn oxidation and substantially diminishing non-radiative recombination, thereby enhancing carrier lifetime and extraction. The -NH_2 hydrogen donor site assists in lowering the ion migration by forming H···I bond and suppressing the generation of the SnI_4 state by acting as a reducing agent. The phenyl ring conjugation of the 4PTSC additive actively contributes to reinforcing the establishment of the preferred crystal growth orientation in perovskite grains. The hydrophobic nature of the 4PTSC additive acts as a barrier to further oxidation of Sn^{2+}, precluding moisture ingress and thus bolstering the stability of the perovskite. Leveraging the multifaceted advantages of the 4PTSC additive, which adeptly controls defect states and the kinetics of crystal growth within Sn-HP, the technology achieves a notable device efficiency of 12.22% (with a certified PCE of 11.70%), an improved V_{oc} of 0.94 V, and an almost imperceptible hysteresis, surpassing the control device PCE of 8.68%. The premier 4PTSC-1.0 PSC has demonstrated superior stability, exceeding 1200 h in ambient air conditions with 30% relative humidity, without the need for encapsulation. Hence, the strategic inclusion of this potent defect passivation technique, endowed with selective functionalities, is advantageous for the elimination of non-radiative recombination pathways, thereby regulating perovskite crystal growth and substantially improving the device's performance and V_{oc} in WBG Sn halide PSCs.

4. Experimental Section

Materials: Indium tin oxide (ITO)-coated glass substrates (AMG, 10 Ω sq^{-1}), acetone (≈99%) and isopropanol (IPA, ≈99.5%) (For substrate cleaning), DMF (99.5%), DMSO (99.8%) (perovskite precursor solvents), Toluene (99.8%) (antisolvent), Dichlorobenzene (99.0%) purchased from Samchun Chemical and chlorobenzene (99% – GR grade, Wako) were used as ETL solvents. Precursor salts, that is, Formamidinium bromide (FABr), Methylammonium bromide (MABr), Phenylethyl ammonium bromide (PEABr) purchased from greatcellsolar, Tin (II) Iodide (SnI_2, sigma-Aldrich) and Tin (II) fluoride (SnF_2, Sigma–Aldrich), 4-Phenylthiosemicarbazide (4PTSC) and thiosemicarbazide (TSC) additive procured from Sigma–Aldrich used without further purification. Poly(3,4-ethylenedioxythiophene) polystyrene sulfonate (PEDOT:PSS, Heraeus Germany) was used as hole transport layer (HTL), Phenyl-C61-butyric acid methyl ester (PCBM, 99.5%, Organic Semiconductor Materials, Republic of Korea) and Bathocuproine (BCP, 99.9%, Alfa Aesar) were used as electron transport layers (ETL). DMF (99.5%, Samchun Chemical) and DMSO (99.8%, Samchun Chemical), toluene (99.8%, Samchun Chemical), and chlorobenzene (CB, 99% – GR grade, Wako) and Dichlorobenzene (Di-CBZ 99.0%, Samchun Chemical) were used as solvents.

Perovskite Precursor Solution Preparation: The perovskite solution was prepared by the mixture of PEABr, FABr, MABr, SnI_2, SnF_2, and Sn in the molar ratio of 0.15: 0.75: 0.10: 1: 0.1: 0.1, and then dissolving in 1 mL of DMF and DMSO mixed solvent (4/1, v/v), followed by stirring at 60 °C for 2 h. For the preparation of the additive-containing precursor solution, 0.5%, 1%, 2% of 4PTSC, and 1% of TSC was added during solution preparation. PCBM solution was prepared with 20 mg mL^{-1} dissolved in CB: DCB mixed solvent in a 1:1 ratio and kept for overnight stirring at room temperature (RT).

Perovskite Solar Cell Fabrication Procedure: ITO-substrates were cleaned with acetone in the ultrasonic bath for 15 min followed by cleaning substrates in acetone and IPA. Substrates were dried in the oven for 10 min at 95 °C to evaporate solvents. Cleaned ITO substrates were UV-Ozone treated for 30 min. In the initial step, PEDOT: PSS (HTL) was coated on substrates at 5000 rpm for 30 s in ambient atmospheric conditions and annealed at 150 °C (20 min) on the hotplate. Later, HTL-coated substrates were transferred inside an N_2-filled glove box prior to perovskite coating. The perovskite films were prepared by spin coating filtered perovskite precursor solution at 8000 rpm for 30 s, followed by antisolvent dripping (200 µL Toluene) at 10th s on perovskite film. These perovskite films were further annealed at 70 °C for 8 min on the hot plate for perovskite crystallization. In the next step electron transport layer (ETL) PCBM spin-coated onto the perovskite film at 1500 rpm for 30 sec and annealed at 70 °C for 5 min, followed by BCP solution coating with 0.5 mg mL^{-1} in IPA solution coated dynamically over PCBM layer at 6000 rpm for 30 s annealed for 10 min at 70 °C on the hot plate. Ag electrodes were deposited through the thermal evaporator under a high vacuum condition (≈3 × 10^{-6} Torr).

Supporting Information

Supporting Information is available from the Wiley Online Library or from the author.

Acknowledgements

The present research was supported by the National Research Foundation of Korea (NRF) funded by the Korea government (MSIT) (NRF- RS-2023-00217270, RS-2023-00212744, and 2023K2A9A2A08000151) and also supported by the GIST Research Institute (GRI) APRI grant funded by the GIST in 2022. This work was supported by the Korea Institute of Energy Technology Evaluation and Planning (KETEP) and the Ministry of Trade, Industry & Energy(MOTIE) of the Republic of Korea (No. RS-2023-00236664).

Conflict of Interest

The authors declare no conflict of interest.

Author Contributions

P.P. and S.C. contributed equally to this work. P.P. performed conceptualization, validation, methodology, investigation, data curation, formal analysis, visualization, and wrote original draft. S.W.C. performed conceptualization, validation, methodology, investigation, data curation, formal analysis, and visualization. J.B. performed formal analysis, resources, data curation, and visualization. S.Y. performed data curation, resources, formal analysis, and visualization. C.-M.O. performed methodology, visualization, and reviewed and edited the author manuscript. I.-W.H. performed methodology, visualization, and reviewed and edited the author manuscript. H.S. performed investigation. H.C. performed formal analysis, visualization, methodology, wrote the original draft and reviewed and edited the author manuscript. S.H. performed resources, visualization, wrote the original draft and reviewed and edited author manuscript. J.S.C. performed visualization, supervision, wrote the original draft and reviewed and edited author manuscript. D.-W.K. performed conceptualization, supervision, project administration, funding acquisition, wrote the original draft and reviewed and edited author manuscript.

Data Availability Statement

The data that support the findings of this study are available from the corresponding author upon reasonable request.

Keywords

4PTSC, chemical coordination, perovskite solar cell, Sn halide perovskite, stability

Received: March 15, 2024
Published online:

[1] P. Verlinden, D. L. Young, G. Xiong, M. O. Reese, L. M. Mansfield, M. Powalla, S. Paetel, R. M. France, P. T. Chiu, N. M. Haegel, *Device* **2023**, *1*, 100013.
[2] a) A. Miyata, A. Mitioglu, P. Plochocka, O. Portugall, J. T.-W. Wang, S. D. Stranks, H. J. Snaith, R. J. Nicholas, *Nat. Phys.* **2015**, *11*, 582; b) V. D'innocenzo, G. Grancini, M. J. Alcocer, A. R. S. Kandada, S. D. Stranks, M. M. Lee, G. Lanzani, H. J. Snaith, A. Petrozza, *Nat. Commun.* **2014**, *5*, 3586.
[3] Z. Xiao, Z. Song, Y. Yan, *Adv. Mater.* **2019**, *31*, 1803792.
[4] J. Lim, M. Kober-Czerny, Y.-H. Lin, J. M. Ball, N. Sakai, E. A. Duijnstee, M. J. Hong, J. G. Labram, B. Wenger, H. J. Snaith, *Nat. Commun.* **2022**, *13*, 4201.
[5] S. E. Sofia, H. Wang, A. Bruno, J. L. Cruz-Campa, T. Buonassisi, I. M. Peters, *Sustainable Energy Fuels* **2020**, *4*, 852.
[6] a) J. Park, J. Kim, H.-S. Yun, M. J. Paik, E. Noh, H. J. Mun, M. G. Kim, T. J. Shin, S. I. Seok, *Nature* **2023**, *616*, 724; b) T. Yang, L. Gao, J. Lu, C. Ma, Y. Du, P. Wang, Z. Ding, S. Wang, P. Xu, D. Liu, *Nat. Commun.* **2023**, *14*, 839; c) NREL solar cell efficiency chart, http://www.nrel.gov/pv/interactivecell-efficiency.html (accessed: July 2023).
[7] a) F. Fu, J. Li, T. C. J. Yang, H. Liang, A. Faes, Q. Jeangros, C. Ballif, Y. Hou, *Adv. Mater.* **2022**, *34*, 2106540; b) W. Chi, S. K. Banerjee, K. Jayawardena, S. R. P. Silva, S. I. Seok, *ACS Energy Lett.* **2023**, *8*, 1535.
[8] a) Z. Liu, C. Zhu, H. Luo, W. Kong, X. Luo, J. Wu, C. Ding, Y. Chen, Y. Wang, J. Wen, *Adv. Energy Mater.* **2023**, *13*, 2203230; b) G. Yang, Z. Ni, Z. J. Yu, B. W. Larson, Z. Yu, B. Chen, A. Alasfour, X. Xiao, J. M. Luther, Z. C. Holman, *Nat. Photonics* **2022**, *16*, 588; c) N. Yan, Y. Gao, J. Yang, Z. Fang, J. Feng, X. Wu, T. Chen, S. Liu, *Angew. Chem., Int. Ed.* **2023**, *62*, 202216668.
[9] a) T. J. Macdonald, L. Lanzetta, X. Liang, D. Ding, S. A. Haque, *Adv. Mater.* **2023**, *35*, 2206684; b) H. Liu, Z. Zhang, W. Zuo, R. Roy, M. Li, M. M. Byranvand, M. Saliba, *Adv. Energy Mater.* **2023**, *13*, 2202209; c) J. Zhao, Z. Zhang, G. Li, M. H. Aldamasy, M. Li, A. Abate, *Adv. Energy Mater.* **2023**, *13*, 2204233.
[10] L. De Trizio, H. Li, A. Casu, A. Genovese, A. Sathya, G. C. Messina, L. Manna, *J. Am. Chem. Soc.* **2014**, *136*, 16277.
[11] a) B. B. Yu, Z. Chen, Y. Zhu, Y. Wang, B. Han, G. Chen, X. Zhang, Z. Du, Z. He, *Adv. Mater.* **2021**, *33*, 2102055; b) G. Liu, X. Jiang, W. Feng, G. Yang, X. Chen, Z. Ning, W. Q. Wu, *Angew. Chem., Int. Ed.* **2023**, *62*, 202305551.
[12] a) M. Chen, G. Kapil, Y. Li, M. A. Kamarudin, A. K. Baranwal, K. Nishimura, S. R. Sahamir, Y. Sanehira, H. Li, C. Ding, *J. Power Sources* **2022**, *520*, 230848; b) M. Chen, G. Kapil, L. Wang, S. R. Sahamir, A. K. Baranwal, K. Nishimura, Y. Sanehira, Z. Zhang, M. A. Kamarudin, Q. Shen, *Chem. Eng. J.* **2022**, *436*, 135196.
[13] X. Jiang, H. Li, Q. Zhou, Q. Wei, M. Wei, L. Jiang, Z. Wang, Z. Peng, F. Wang, Z. Zang, *J. Am. Chem. Soc.* **2021**, *143*, 10970.
[14] H. Zhang, L. Pfeifer, S. M. Zakeeruddin, J. Chu, M. Grätzel, *Nat. Rev. Chem.* **2023**, *7*, 632.
[15] a) S. Cho, P. Pandey, J. Park, T.-W. Lee, H. Ahn, H. Choi, D.-W. Kang, *Chem. Eng. J.* **2022**, *446*, 137388; b) G. Liu, Y. Zhong, W. Feng, M. Yang, G. Yang, J. X. Zhong, T. Tian, J. B. Luo, J. Tao, S. Yang, *Angew. Chem.* **2022**, *134*, 202209464; c) C. Duan, F. Zou, Q. Wen, M. Qin, J. Li, C. Chen, X. Lu, L. Ding, K. Yan, *Adv. Mater.* **2023**, *35*, 2300503.
[16] Q. Tai, X. Guo, G. Tang, P. You, T. W. Ng, D. Shen, J. Cao, C. K. Liu, N. Wang, Y. Zhu, *Angew. Chem., Int. Ed.* **2019**, *58*, 806.
[17] a) J. Liu, S. Wang, W. Zhu, Z. Tang, L. Ding, F. Hao, *Chem. Eng. J.* **2023**, *453*, 139975; b) S. Wang, L. Yan, W. Zhu, Z. Cao, L. Zhou, L. Ding, F. Hao, *Nano Energy* **2022**, *99*, 107416; c) B. Li, H. Di, B. Chang, R. Yin, L. Fu, Y. N. Zhang, L. Yin, *Adv. Funct. Mater.* **2021**, *31*, 2007447.
[18] a) Y. Liao, H. Liu, W. Zhou, D. Yang, Y. Shang, Z. Shi, B. Li, X. Jiang, L. Zhang, L. N. Quan, *J. Am. Chem. Soc.* **2017**, *139*, 6693; b) Y. Han, S. Park, C. Kim, M. Lee, I. Hwang, *Nanoscale* **2019**, *11*, 3546.
[19] a) K. Cao, Y. Huang, M. Ge, F. Huang, W. Shi, Y. Wu, Y. Cheng, J. Qian, L. Liu, S. Chen, *ACS Appl. Mater. Interfaces* **2021**, *13*, 26013; b) W. Zhou, D. Li, Z. Xiao, Z. Wen, M. Zhang, W. Hu, X. Wu, M. Wang, W. H. Zhang, Y. Lu, *Adv. Funct. Mater.* **2019**, *29*, 1901026; c) X. Hou, S. Huang, W. Ou-Yang, L. Pan, Z. Sun, X. Chen, *ACS Appl. Mater. Interfaces* **2017**, *9*, 35200.
[20] P. Pandey, A. Sengupta, S. Parmar, U. Bansode, S. Gosavi, A. Swarnkar, S. Muduli, A. D. Mohite, S. Ogale, *ACS Appl. Nano Mater.* **2020**, *3*, 3305.
[21] R. Arivazhagan, C. Sridevi, A. Prakasam, *J. Mol. Struct.* **2021**, *1232*, 129956.
[22] J. Bahadur, S. Cho, P. Pandey, J. Ryu, S. Yoon, D.-G. Lee, J. T. Song, J. S. Cho, D.-W. Kang, *Appl. Surf. Sci.* **2023**, *637*, 157901.
[23] D. Meggiolaro, D. Ricciarelli, A. A. Alasmari, F. A. Alasmary, F. De Angelis, *J. Phys. Chem. Lett.* **2020**, *11*, 3546.

[24] a) S. Sazeli, A. R. Nath, M. H. Ahmad, N. W. M. Zulkifli, M. R. Johan, W. A. Yehye, L. H. Voon, *RSC Adv.* **2021**, *11*, 7138; b) B. Ali, K. M. Khan, S. Hussain, S. Hussain, M. Ashraf, M. Riaz, A. Wadood, S. Perveen, *Bioorg. Chem.* **2018**, *79*, 34; c) V. A. Kumar, Y. Sarala, A. Siddikha, S. Vanitha, S. Babu, A. V. Reddy, *J Appl Pharm Sci* **2018**, *8*, 071.
[25] S. Joy, H. R. Atapattu, S. Sorensen, H. Pruett, A. B. Olivelli, A. J. Huckaba, A.-F. Miller, K. R. Graham, *Energy Environ. Sci.* **2022**, *10*, 13278.
[26] S. Wafee, B. H. Liu, C.-C. Leu, *Mater. Today Energy* **2021**, *22*, 100847.
[27] S. Chen, X. Xiao, H. Gu, J. Huang, *Sci. Adv.* **2021**, *7*, eabe8130.
[28] J. Cao, H. L. Loi, Y. Xu, X. Guo, N. Wang, C. k. Liu, T. Wang, H. Cheng, Y. Zhu, M. G. Li, *Adv. Mater.* **2022**, *34*, 2107729.
[29] a) D. Thrithamarassery Gangadharan, D. Valverde-Chavez, A.-F. Castro-Mendez, V. Prakash, R. Izquierdo, C. Silva, D. Ma, J.-P. Correa-Baena, *ACS Appl. Energy Mater.* **2021**, *4*, 2616; b) D. Thrithamarassery Gangadharan, P. Li, Q. Zhang, F. Yang, R. Izquierdo, B. Sun, D. Ma, *Energy Technol.* **2021**, *9*, 2100176.
[30] P. Kour, M. Chenna Reddy, S. Pal, S. Sidhik, T. Das, P. Pandey, S. P. Mukherjee, S. Chakraborty, A. D. Mohite, S. Ogale, *Angew. Chem., Int. Ed.* **2021**, *60*, 18750.
[31] Z. Zhao, F. Gu, Y. Li, W. Sun, S. Ye, H. Rao, Z. Liu, Z. Bian, C. Huang, *Adv. Sci.* **2017**, *4*, 1700204.
[32] a) Y. Li, M. Dailey, P. J. Lohr, A. D. Printz, *Energy Environ. Sci.* **2021**, *9*, 16281; b) X. Zhou, L. Zhang, H. Hu, Z. Jiang, D. Wang, J. Chen, Y. Li, J. Wu, Y. Zhang, M. Zhang, *Nano Energy* **2022**, *104*, 107988; c) Y. Che, Z. Liu, Y. Duan, J. Wang, S. Yang, D. Xu, W. Xiang, T. Wang, N. Yuan, J. Ding, *Angew. Chem., Int. Ed.* **2022**, *61*, 202205012.
[33] a) Y.-J. Kang, S.-I. Na, *Nano Energy* **2022**, *97*, 107193; b) J. Kim, A. J. Yun, B. Gil, Y. Lee, B. Park, *Adv. Funct. Mater.* **2019**, *29*, 1905190; c) Q. Cao, J. Yang, T. Wang, Y. Li, X. Pu, J. Zhao, Y. Zhang, H. Zhou, X. Li, X. Li, *Energy Environ. Sci.* **2021**, *14*, 5406.
[34] a) L. Zhu, R. Zhao, R. Zhuang, T. Wu, L. Xie, Y. Hua, *EcoMat* **2023**, *5*, 12313; b) B. Han, S. Yuan, T. Fang, F. Zhang, Z. Shi, J. Song, *ACS Appl. Mater. Interfaces* **2020**, *12*, 14224.
[35] a) C. Li, S. Tscheuschner, F. Paulus, P. E. Hopkinson, J. Kießling, A. Köhler, Y. Vaynzof, S. Huettner, *Adv. Mater.* **2016**, *28*, 2446; b) S. Tan, T. Huang, Y. Yang, *J. Phys.:Energy* **2021**, *3*, 042003.
[36] Y. Tao, Z. Liang, J. Ye, H. Xu, G. Liu, D. Aldakov, X. Pan, P. Reiss, X. Tian, *Small* **2023**, *19*, 2207480.
[37] L. Liu, A. Mei, T. Liu, P. Jiang, Y. Sheng, L. Zhang, H. Han, *J. Am. Chem. Soc.* **2015**, *137*, 1790.
[38] X. Yang, J. Han, W. Ruan, Y. Hu, Z. He, X. Jia, S. Zhang, D. Wang, *Chin. Chem. Lett.* **2022**, *33*, 1425.